

**Sulfur isotope behavior during metamorphism and anatexis of Archean sedimentary rocks:
a case study from the Ghost Lake batholith, Ontario, Canada**

Claire E. Bucholz¹*, Joseph A. Biasi¹, Patrick Beaudry², and Shuhei Ono²

¹California Institute of Technology, Pasadena, CA 91125

²Massachusetts Institute of Technology, Cambridge, MA 02139

*cbucholz@caltech.edu

SUBMITTED TO EARTH and PLANETARY SCIENCE LETTERS

REVISION #1

1 **ABSTRACT**

2 Recycling of surface-derived sulfur into the deep earth can impart distinct sulfur isotope
3 signatures to magmas. The details of sulfur transfer from sedimentary rocks to magmas (and
4 ultimately igneous rocks) through metamorphism and devolatilization and/or partial melting,
5 however, is difficult to trace. To understand this process in detail we studied multiple-sulfur
6 isotope compositions of sulfides in the Archean (*c.* 2685 Ma) Ghost Lake batholith (GLB) and its
7 surrounding host metasedimentary rocks of the Superior Craton (Ontario, Canada) by high
8 spatial resolution secondary ion mass spectrometry, complemented by high-precision gas source
9 isotope ratio mass spectrometry measurements. The GLB comprises strongly peraluminous
10 biotite+cordierite, biotite+muscovite, and muscovite+garnet+tourmaline granites to
11 leucogranites, which are thought to represent the partial melts of surrounding metagreywackes
12 and metapelites. The metasedimentary rocks display a range of metamorphic grades increasing
13 from biotite-chlorite (280-380°C) at ~5 km away from the GLB to sillimanite-K-feldspar grade
14 (~660°C) immediately adjacent to the batholith, thus providing a natural experiment to
15 understand sulfur isotope variations from low- to high-grade Archean sedimentary rocks, as well
16 as granites representative of their partial melts.

17 We find that metasedimentary sulfide $\delta^{34}\text{S}$ values increase with progressive
18 metamorphism at most 2-3‰ (from -1‰ up to +1 to +2‰). An increase in $\delta^{34}\text{S}$ values in
19 pyrrhotite during prograde metamorphism can be explained through Rayleigh fractionation
20 during pyrite desulfidation reactions. Pyrite from all but one of the granite samples preserve $\delta^{34}\text{S}$
21 values similar to that of the high-grade metasedimentary rocks, indicating that partial melting did
22 not result in significant fractionation of $\delta^{34}\text{S}$. The exception to this is one granite sample from a
23 part of the batholith characterized by abundant metasedimentary inclusions. This sample contains

24 pyrite with heterogeneous and low $\delta^{34}\text{S}$ values (down to -16‰) which likely resulted from
25 incomplete homogenization of sulfur between the granitic melt and metasedimentary inclusions.
26 Small (several tenths of a permil), mostly positive $\Delta^{33}\text{S}$ are observed in both the
27 metasedimentary rocks and granites.

28 Our results suggest that Archean strongly peraluminous granites could be a high-fidelity
29 archive to quantify the bulk sulfur isotope composition of the Archean siliciclastic sediments.
30 Further, our findings indicate that subduction of reduced sulfur-bearing sediments in the Archean
31 with $\delta^{34}\text{S}$ at or near 0‰ should result in release of sulfur-bearing fluids in the mantle wedge with
32 similar values (within a few permil). S-MIF (if initially present in Archean surface material) may
33 be preserved during this process. However, the absence of S-MIF in igneous rocks does not
34 preclude assimilation of Archean sedimentary material as either S-MIF may not be originally
35 present in the Archean sedimentary sulfur and/or homogenization or dilution could obscure any
36 S-MIF originally present in assimilated Archean sediments.

37

38 1. Introduction

39 Atmospheric oxygen levels increased throughout Earth's history with the largest increase
40 in O_2 levels occurring during the "Great Oxidation Event" (GOE, ~2.4-2.3 Ga; Canfield, 2004)
41 from $<10^{-5}$ to 1-10% of the present atmospheric level. One of the most distinctive chemical
42 fingerprints of low atmospheric O_2 levels is the presence of mass-independent fractionation
43 (MIF) of sulfur isotopes in Archean and earliest Paleoproterozoic sedimentary sulfide and sulfate
44 arising from SO_2 photodissociation in a low- pO_2 atmosphere (see review of Ono, 2017; Fig.

45 1a,b). Although the details of the gas phase atmospheric chemistry leading to non-zero $\Delta^{33}\text{S}^1$ are
46 not fully understood (*c.f.*, Ono et al., 2017), a leading model for the Archean sulfur cycle is that
47 reduced and elemental sulfur species acquired positive $\Delta^{33}\text{S}$, whereas oxidized sulfur (sulfate)
48 carried the complementary negative $\Delta^{33}\text{S}$ (*e.g.*, Farquhar and Wing, 2003; Halevy et al., 2010).

49 Similarly, sulfur isotopes in igneous rocks have been used as tracer of assimilation of
50 oxidized or reduced sedimentary sulfur. For example, magnetite-series, or relatively oxidized,
51 granitoids have positive bulk-rock $\delta^{34}\text{S}$ values of +1 to +9‰, whereas ilmenite-series granitoids
52 have predominantly negative values between -11 and +1‰ (*e.g.*, Ishihara and Sasaki, 1989). The
53 positive $\delta^{34}\text{S}$ of magnetite-series granitoids was interpreted as a result of incorporation of sulfur
54 derived from subducted sulfate-bearing sediments or seawater, whereas the negative $\delta^{34}\text{S}$ of
55 ilmenite-series granitoids was attributed to assimilation of sulfur from reduced graphite- and
56 sulfide-bearing sediments. Multiple sulfur isotopes have also been measured in igneous rocks as
57 a tracer of Archean sulfur in magmas. For example, Bekker et al. (2009) found non-zero $\Delta^{33}\text{S}$ in
58 sulfides from Archean komatiite-hosted Fe-Ni sulfide deposits and concluded that the komatiite
59 magmas gained sulfur from Archean seafloor hydrothermal sulfides and sulfur-rich shales (Fig.
60 1c). Similarly, metamorphosed ultramafic sills, gabbros, and tonalites from the >3.8 Ga
61 Nuvvuagittuq Greenstone Belt (Quebec) have $\Delta^{33}\text{S}$ values from -0.03 to 0.26‰, consistent with
62 having mostly mantle-derived sulfur ($\Delta^{33}\text{S}=0$), but also a minor contribution from surrounding
63 metasedimentary rocks (Thomassot et al., 2015; Fig. 1c). Similarly, positive $\Delta^{33}\text{S}$ have been
64 observed in Proterozoic igneous rocks such as the Bushveld Complex of South Africa
65 (Penniston-Dorland, 2008; 2012; Magalhães et al., 2018; 2019) and granitoids from Australia

¹ S isotope ratios are expressed as $\delta^{\text{x}}\text{S} = \{(\text{xS}/\text{S}^{32})_{\text{sample}}/(\text{xS}/\text{S}^{32})_{\text{CDT}} - 1\} * 1000$ (‰), where x is 33, 34, or 36 & CDT is Canyon Diablo meteorite troilite (Ding et al., 2001). $\Delta^{\text{x}}\text{S}$ is the ‰ deviation from the mass dependent relationship: $\Delta^{\text{x}}\text{S} = 1000 [\ln(\frac{\delta^{\text{x}}\text{S}}{1000} + 1) - \theta \ln(\frac{\delta^{34}\text{S}}{1000} + 1)]$. $\theta = 0.515$ for ^{33}S & 1.90 for ^{36}S (for discussion of Δ definition see Ono, 2017).

66 (LaFlamme et al., 2018; Selvaraja et al., 2017; Fig. 1c). S-MIF has also been observed in
67 magmatic sulfides in modern ocean island basalts (OIB) from Mangaia, Cook Islands (Cabral et
68 al., 2013) and Pitcairn Island (Delavault et al., 2016). For these OIB samples, both $\delta^{34}\text{S}$ and $\Delta^{33}\text{S}$
69 values are mostly negative (Fig. 1c) and interpreted as evidence for deeply subducted Archean
70 altered oceanic crust. (We note, however, that the majority of sulfur isotope studies of OIBs have
71 observed $\Delta^{33}\text{S} = 0$ [e.g., Discovery/Shona: Labidi et al., 2013; Samoa: Labidi et al., 2015; Dottin
72 et al., 2020; Canary: Beaudry et al., 2018; Fig. 1c]). In contrast to some OIB, S-MIF observed in
73 sulfide inclusions in diamonds exhibit primarily positive $\Delta^{33}\text{S}$ values (Farquhar et al., 2002;
74 Thomassot et al., 2009; Smit et al., 2019; Fig. 1c). Based on these findings, it has been suggested
75 that the material in some OIB source regions represents a complementary oxidized ($\Delta^{33}\text{S} < 0$)
76 sulfur reservoir (through sulfate reduction during ocean-floor basalt alteration) to that of the
77 reduced ($\Delta^{33}\text{S} > 0$) subcontinental lithospheric source of diamonds (Cabral et al., 2013).

78 However, our understanding of sulfur transfer from Archean surface reservoirs to the igneous
79 rock records remains limited in that existing multiple sulfur isotope data for igneous materials are
80 from samples which represent a mixture of different reservoirs (*i.e.*, mantle and Archean
81 sediment/oceanic crust). In addition, the process of sulfur transfer from sedimentary rocks to
82 magmas is poorly understood. During metamorphism, partial melting, and/or assimilation,
83 desulfidation of sedimentary pyrite produces pyrrhotite and sulfur-bearing fluids (Ferry, 1981;
84 Tomkins, 2010). Thermodynamic calculations and experiments indicate that this reaction begins
85 at $\sim 75\text{--}200^\circ\text{C}$ and subsequently evolves with increasing temperature along the pyrrhotite-pyrite
86 buffer (Toulmin and Barton, 1964). The loss of sulfur from pyrite or pyrrhotite to fluids can drive
87 several per mil fractionations between the $\delta^{34}\text{S}$ of residual sulfide and fluid, which may be
88 preserved in the sulfur isotope composition of melts formed through partial melting or assimilation

89 of metasedimentary rocks. Although sulfur transfer from sedimentary rock to melt should not
90 disturb the original sedimentary $\Delta^{33}\text{S}$, non-zero $\Delta^{33}\text{S}$ can be diluted by external sulfur or
91 homogenized during metamorphism (e.g., Cui et al., 2018). Consequently, a magma assimilating
92 S-MIF-bearing sedimentary sulfur, may or may not preserve S-MIF signals.

93 If $\Delta^{33}\text{S}$ - $\delta^{34}\text{S}$ variations are to be used in igneous rocks to trace contamination by Archean
94 sedimentary material, this process must be understood in a fundamental way. Here we present a
95 case study of the Ghost Lake batholith, an Archean strongly peraluminous granite (SPG; *i.e.*,
96 bulk-rock molar $\text{Al}/(2\text{Ca}-1.67\text{P}+\text{Na}+\text{K})>1.1$) and its host metasedimentary rocks. The Al-rich
97 compositions of SPGs indicate derivation predominantly (if not completely) through the partial
98 melting of metasedimentary rocks (see discussion in Bucholz and Spencer, 2019) and therefore
99 are a useful archive to understand how sulfur isotopes from sedimentary rocks are transferred to
100 the igneous rock record. We analyzed sulfur isotopes for sulfides from both metasedimentary
101 rocks representative of the granite source and from the granite itself. We interpret these results in
102 the context of metamorphic grade, modeling of devolatilization reactions, and sulfur transfer
103 between high temperature fluids and melts.

104

105 **2. Geologic setting**

106 The Ghost Lake batholith (GLB) is situated in the Sioux Lookout terrane at the Winnipeg
107 River-Wabigoon subprovince boundary of the Superior Province (Fig. 2a). The Sioux Lookout
108 terrane comprises (a) metasedimentary (Zealand/Minnitaki/Warclub Units) and metavolcanic
109 assemblages that were deposited at ~ 2730 - 2700 Ma (Blackburn et al., 1991) and (b) a 150-km-
110 long belt of peraluminous granite plutons, including the GLB, which is the largest (~ 220 km 2 in
111 areal extent) (Breaks and Moore, 1992). The Zealand Unit is characterized by east-striking

112 foliations, a range in metamorphic grades (Fig. 2a-c), and zones of incipient migmatization
113 (Breaks and Moore, 1992; Fig. 2d). Metamorphic grade in the metasedimentary units increases
114 northward from the Wabigoon subprovince with mineral isograds of chlorite±biotite, andalusite,
115 garnet, sillimanite-muscovite, and sillimanite-K-feldspar (Breaks and Moore, 1992; Fig. 2a). The
116 metamorphic gradient calculated based on mineral assemblages and thermobarometry increases
117 steeply northward (50°C/km) from the low-grade Wabigoon subprovince (~200°C) to the
118 margins of the GLB (>700°C) at a constant pressure of ~0.3 GPa (Breaks and Moore, 1992). On
119 the west-northwest batholith margins, clastic sedimentary rocks were metamorphosed
120 sufficiently as to partially melt (Fig. 2d). In contrast, host rocks to the east and south contain
121 mineral assemblages characteristic of the sillimanite-muscovite zone, but do not preserve
122 evidence for incipient melting (Fig. 2a).

123 The GLB consists of eight units comprising a volumetrically-dominant,
124 biotite(±cordierite±muscovite) granite (GLB-1/-2 of Breaks and Moore, 1992), lesser amounts of
125 locally garnet-bearing biotite+muscovite granite (GLB-3), and highly evolved,
126 tourmaline+garnet+muscovite-bearing pegmatitic granitic facies (GLB-4 to -8) found primarily
127 in the eastern lobe of the GLB. Samples from units GLB-1, -2, and -4 were selected for study.
128 The western and central part of the GLB is weakly foliated and contains zones with abundant
129 inclusions of metasedimentary rocks and restitic material (Fig. 2a,f). To the east, the intensity of
130 foliation and abundance of the inclusions decrease to the point that the batholith is either massive
131 or preserves original magmatic layering. However, locally on the batholith's eastern margin,
132 there are zones rich in partially melted, sedimentary inclusions (Fig. 2e).

133 A detailed examination of the petrology and bulk-rock chemistry of the GLB was
134 presented by Breaks and Moore (1992), who proposed the following petrogenetic model.

135 Greywackes and mudstones (the Zealand unit) were deposited as turbidites in an arc-proximal
136 basin between 2730-2700 Ma. Subsequently, during collision between an arc (the Wabigoon
137 subprovince) and a microcontinent (the Winnipeg River subprovince), the sediments were
138 metamorphosed under high-temperature, low-pressure conditions resulted in anatexis and
139 widespread production of peraluminous granitic melts (*c.* 2685 Ma). The metasedimentary rocks
140 preserved along the margins of the GLB are thought to be representative of the source rock for
141 the batholith.

142

143 **3. Analytical and methods**

144 Petrographic descriptions of both metasedimentary and granitic samples are given in the
145 Supplementary Material. Bulk-rock major and trace elements were measured via X-ray
146 fluorescence (XRF) for pseudosection construction and are given in Table S1. Sulfide and
147 silicate mineral major and minor elements were analyzed via electron microprobe analysis
148 (EMPA). Mineral compositions are reported in Table S2 and S3. Sample average sulfide
149 analyses are given in Table 2. XRF and EMPA analytical methods and pseudosection
150 construction details are given in the Supplementary Material.

151

152 *3.1 Sulfur isotope analysis*

153 3.1.1 Secondary ion mass spectrometry

154 Sulfur isotopes (^{32}S , ^{33}S , ^{34}S) of sulfide separates (see Supplemental Material) were
155 analyzed on a Cameca 7f-GEO ion microprobe (Caltech). A primary Cs^+ beam of ~ 3 nA rastered
156 over an area of $\sim 20 \times 20 \mu\text{m}$ during pre-sputtering (90 s) and then over a $5 \times 5 \mu\text{m}$ area during data
157 collection was used. As the 7f-GEO lacks a multi-collection setup, ^{32}S was measured on one

158 Faraday cup and ^{33}S and ^{34}S were measured on a second Faraday cup sequentially, in rapid peak-
159 jumping mode. 30 cycles of sequential mass measurements were collected per spot analysis. A
160 mass resolving power of ~ 3900 was used to resolve ^{33}S from ^{32}S . Sample analyses were
161 bracketed by standard measurements every 15-20 measurements. During analysis of pyrite, we
162 measured three different pyrite standards; Balmat ($\delta^{34}\text{S} = 16.4\text{\textperthousand}$; Kozdon et al., 2010), Ruttan
163 ($\delta^{34}\text{S} = 1.2\text{\textperthousand}$; Crowe and Vaughan, 1996), and Orocampa pyrite ($\delta^{34}\text{S} = 3.41\text{\textperthousand}$, $\delta^{33}\text{S} = 1.74$; these
164 values differ from those of Fischer et al. (2014) which were found to be in error during this
165 study). During analysis of pyrrhotite we measured Anderson pyrrhotite ($\delta^{34}\text{S} = 1.4 \pm 0.2\text{\textperthousand}$; Crowe
166 and Vaughan, 1996) and Orocampa pyrite. Raw isotope ratios were then corrected for
167 instrumental mass fractionation (IMF, see Supplementary Material for details) using Orocampa
168 pyrite and Anderson pyrrhotite as primary standards.

169 In-run precision (2σ , over 30 cycles on the same spot) were $\sim 0.02\text{\textperthousand}$ for $\delta^{34}\text{S}$ and $\sim 0.06\text{\textperthousand}$
170 for $\delta^{33}\text{S}$. External precision, defined as the 1σ of multiple (3-6) adjacent measurements of
171 standards was $\delta^{34}\text{S} = 0.06\text{--}0.55\text{\textperthousand}$, $\delta^{33}\text{S} = 0.13\text{--}0.58\text{\textperthousand}$, and $\Delta^{33}\text{S} = 0.13\text{--}0.56\text{\textperthousand}$. Full analyses of
172 standards and unknowns (both uncorrected and corrected for IMF) are in Tables S3 and S4.

173

174 3.2.2 Isotope ratio mass spectrometry

175 Separated sulfides from 7 samples were reacted in a chromous chloride (CrCl_2) solution
176 to extract acid volatile sulfur (e.g., pyrrhotite) and chromium reducible sulfur (e.g., pyrite)
177 species following Canfield et al. (1986). The reaction was performed under an N_2 atmosphere for
178 2 hours and the evolved H_2S gas was trapped in a zinc acetate solution and precipitated as zinc
179 sulfide (ZnS). Silver nitrate (AgNO_3) was then added to recover silver sulfide solids (Ag_2S),
180 which were centrifuged and then dried at 80°C and weighed. The Ag_2S precipitates weighed

181 between 0.16 to 2.68 mg (Table S5) and were fluorinated for over 8 h at 300°C. The produced
182 SF₆ was purified with a gas chromatograph by sequentially going through a column packed with
183 molesieve 5 Å, followed by a column packed with HayeSep Q. The purified SF₆ gas was
184 transferred to the Thermo-electron MAT 253 isotope ratio mass spectrometer (IRMS) at MIT,
185 where ion beams of ³²SF₅⁺, ³³SF₅⁺, ³⁴SF₅⁺ and ³⁶SF₅⁺ were measured, as previously described
186 (Ono et al., 2006; 2012).

187 Replicate analyses of reference sulfide material (IAEA-S1) by Ono et al. (2012) yielded -
188 0.30±0.26‰, 0.100±0.014‰, and -0.57±0.19‰ for $\delta^{34}\text{S}$, $\Delta^{33}\text{S}$, and $\Delta^{36}\text{S}$, respectively (n=28, 2 σ)
189 for 2 mg Ag₂S. Fluorination of small IAEA-S1 samples (40 to 130 µg Ag₂S, N=13) by Fortin et
190 al. (2019) yielded standard deviations (2 σ) of 0.43, 0.03, and 0.54‰ for $\delta^{34}\text{S}$, $\Delta^{33}\text{S}$ and $\Delta^{36}\text{S}$,
191 respectively. The overall precision of isotope ratio analyses is between those values (*i.e.*, 0.26 to
192 0.43‰ for $\delta^{34}\text{S}$), with larger standard deviation for smaller samples. During our analyses, our
193 IAEA-S1 bracketing standards (2 mg Ag₂S) yielded an average of -0.26±0.20‰, 0.093±0.004‰,
194 and -0.56±0.06‰ for $\delta^{34}\text{S}$, $\Delta^{33}\text{S}$, and $\Delta^{36}\text{S}$, respectively (n = 3, 2 σ), in agreement with Ono et al.
195 (2012). Mass-spectrometer precisions, evaluated by repeated (n=7) measurement cycles, are
196 from 0.01-0.15 ‰ for $\delta^{34}\text{S}$, 0.01-0.04 ‰ for $\Delta^{33}\text{S}$ and 0.04-0.5 ‰ for $\Delta^{36}\text{S}$ (all 1 σ), generally
197 increasing for smaller samples (Table S5).

198

199 **4. Results**

200 *4.1 Sulfide major and minor element compositions*

201 The only observed sulfide mineral in the granites is pyrite (Fig. 3b). In the
202 metasedimentary rocks, one biotite-chlorite grade sample (SP-18-10) and one sillimanite-K-
203 feldspar grade sample (SP-18-27) contain pyrite as the dominant sulfide phase. Pyrite in the

204 latter sample likely formed during retrogression of pyrrhotite upon cooling (Craig and Volkes,
205 1993). All other metasedimentary samples contained pyrrhotite (Fig. 3a) as the primary sulfide
206 with stoichiometries ranging from $\text{Fe}_{0.88}\text{S}$ to $\text{Fe}_{0.94}\text{S}$. No systematic variation in stoichiometry
207 was observed with increasing metamorphic grade. Minor chalcopyrite was observed in a few
208 metasedimentary samples (Fig. 3a). Otherwise, Ni, Cu, and Zn were present at <0.2 wt.% in all
209 sulfides.

210

211 *4.2 Pressure-temperature estimates – thermobarometry and pseudosections*

212 A maximum pressure during metamorphism of ~0.4 GPa is inferred from the presence of
213 andalusite in the andalusite- and garnet-grade samples (Fig. 4). In the high-grade metamorphic
214 zones, metamorphic pressures are constrained to be below 0.35 GPa based on the intersection of
215 the univariant reaction curves muscovite + plagioclase + quartz = K-feldspar + Al_2SiO_5 + H_2O
216 and the water-saturated peraluminous granite solidus (Holtz et al., 1992, Fig. 4). Evidence for
217 this constraint comes from the coexistence of sillimanite and K-feldspar in metapelitic rocks
218 lacking evidence for partial melting.

219 The increase in metamorphic gradient northward is primarily a reflection of increasing
220 temperature. Three metasedimentary samples from the biotite-chlorite zone contain
221 prehnite/pumpellyite indicating temperatures of ~275-380°C. Minimum temperatures of the
222 rocks of the andalusite isograd are defined by the reaction of pyrophyllite = andalusite + quartz +
223 H_2O , corresponding to 400°C at 0.3 GPa and maximum temperatures of ~550°C are constrained
224 by the reaction andalusite = sillimanite (Fig. 4). Garnet-biotite thermometry (Holdaway, 2000)
225 from four samples above the garnet isograd yielded temperatures of 510-585°C (Table 1).
226 Metamorphic temperatures above the first sillimanite isograd (sillimanite+muscovite) are

227 constrained by the reactions andalusite = sillimanite (~550°C) and muscovite + plagioclase +
228 quartz = K-feldspar + Al_2SiO_5 + H_2O (~625 °C, Thompson and Tracy, 1979) at 0.3 GPa (Fig. 4).
229 Samples in the sillimanite-K-feldspar zone crystallized between 625°C (see constraint for K-
230 feldspar-muscovite samples) and the water-saturated peraluminous granite solidus (660 °C, Holtz
231 et al., 1992).

232 Best temperature estimates at 0.3 GPa via pseudosection analysis confirms the constraints
233 above (Table 1, Supplemental Material). Briefly, phase assemblages of biotite+chlorite-,
234 andalusite-, garnet-, and sillimanite-K-feldspar-grade metasedimentary rocks are reproduced
235 over a range of 280-380°C, 420-550°C, and ~660°C, respectively.

236

237 *4.3 SIMS sulfur isotope analysis*

238 4.3.1 Note on IMF correction for pyrrhotite

239 Well-characterized, homogeneous, matrix-matched standards are critical for precise and
240 accurate SIMS analysis (Kozdon et al., 2010). Pyrrhotite presents a particular challenge in that it
241 is non-stoichiometric with a generalized formula of Fe_{1-x}S ($x = 0-0.2$). Anderson pyrrhotite, the
242 standard used in this study, has a reported major element composition of $\text{Fe}_{0.88(\pm 0.01)}\text{S}$ (Kozdon et
243 al., 2010) which we confirmed (average measured values: $\text{Fe} = 59.58 \pm 0.32$ wt.%, $\text{S} = 39.98 \pm 0.29$
244 wt.%, $\text{Fe}/\text{S} = 0.88 \pm 0.01$, all errors 1σ). Pyrrhotite from our samples, however, displays a range
245 of Fe/S values from 0.88 to 0.94, raising the question whether the Anderson pyrrhotite is an
246 appropriate matrix-matched standard. To assess whether our sample pyrrhotite ionized and
247 sputtered similarly to the standard pyrrhotite, we compared yields (defined as $^{32}\text{S}^-$ counts per
248 second per nA of primary beam current) of the standard and unknowns (Fig. S9). For the
249 majority of pyrrhotite-bearing samples (~75%), the $^{32}\text{S}^-$ yields fell within the range of Anderson

250 pyrrhotite yields from the same analytical session, supporting the assumption that the standards
251 and unknowns were sputtering and ionizing in a similar fashion. In addition, these samples
252 yielded the same values within uncertainty of the IRMS data. However, for 3 samples (see Table
253 2), the unknown pyrrhotite $^{32}\text{S}^-$ yields were either higher or lower than that of the Anderson
254 pyrrhotite, suggesting potentially different matrix effects. Therefore, for these latter samples
255 (indicate in Table 2) there is uncertainty in the accuracy of the corrected $\delta^{34}\text{S}$ and $\delta^{33}\text{S}$ values.
256 However, $\Delta^{33}\text{S}$ values are robust even with non-matrix matched standards/samples.

257 Additionally, in 5 samples, $^{32}\text{S}^-$ SIMS yields were correlated with raw $^{34}\text{S}/^{32}\text{S}$ ratios
258 suggesting strong matrix effects during the ionization and sputtering, potentially due to mixed
259 phases present in the sulfides resulting from incomplete breakdown of pyrite to pyrrhotite or
260 retrograde conversion of pyrrhotite to pyrite. Although we report data for these samples,
261 corrected $\delta^{34}\text{S}$ and $\delta^{33}\text{S}$ may not be accurate as we were unable to confidently construct an
262 empirical IMF correction (see Table 2). Due to these uncertainties, we only discuss pyrrhotite
263 SIMS data where (a) yields were similar to Anderson pyrrhotite and (b) no correlation between
264 $^{32}\text{S}^-$ yields with $^{34}\text{S}/^{32}\text{S}$ ratios were observed.

265

266 *4.3.2 Sulfides from metasedimentary rocks and granites*

267 Pyrrhotite from 7 biotite-chlorite grade samples display a range of $\delta^{34}\text{S}$ values of -2.5 to
268 1.3‰ with an average of $-0.7 \pm 0.8\text{‰}$ (1σ , Fig. 5a). Only two samples from the andalusite isograd
269 (SP-16-36, SP-16-42) yielded robust SIMS $\delta^{34}\text{S}$ values with sample averages of $2.5 \pm 0.2\text{‰}$ and -
270 $2.6 \pm 0.4\text{‰}$ (1σ), respectively (Fig. 5b). Garnet and K-feldspar-sillimanite grade samples have
271 pyrrhotite $\delta^{34}\text{S}$ values between -2.1 to +1.3‰ (Fig. 5c,d). $\Delta^{33}\text{S}$ values for the majority of
272 analyzed sulfides are within uncertainty of zero (± 0.4 to 1.0‰ , 2σ).

273 Pyrite from the three granite samples have sample average $\delta^{34}\text{S}$ values of 0.6 ± 0.6 ,
274 1.2 ± 0.3 , and $0.7\pm0.1\text{\textperthousand}$ (1σ) (Fig. 5e, Fig. 6a). Pyrite from one granite sample (SP-16-22)
275 displays isotopically light and heterogeneous inter-grain $\delta^{34}\text{S}$ values from -0.5 to $-16.4\text{\textperthousand}$. $\Delta^{33}\text{S}$
276 values for most analyzed sulfides were within 2σ uncertainty of zero, but are mostly positive
277 (Fig. 6a).

278

279 *4.4 IRMS sulfur isotopes*

280 $\delta^{34}\text{S}$ values of sulfides increase with increasing metamorphic grade (see circles in Fig. 5),
281 from -1.1 and $-2.0\text{\textperthousand}$ in the biotite-chlorite and andalusite-grade samples to 1.1 to $1.7\text{\textperthousand}$ in the
282 garnet and K-feldspar—sillimanite grade samples. $\delta^{34}\text{S}$ values in pyrite from the two analyzed
283 granite samples are 0.5 and $1.7\text{\textperthousand}$ (1σ). $\Delta^{33}\text{S}$ values for the granites and the metasedimentary
284 rocks vary from -0.09 to $+0.43\text{\textperthousand}$ (Fig. 6 and 7). For example, biotite-chlorite grade sample SP-
285 18-8 has $\Delta^{33}\text{S}$ of $0.43\pm0.03\text{\textperthousand}$ and both granites have small, positive $\Delta^{33}\text{S}$ ($+0.08$ and $0.16\text{\textperthousand}$,
286 Fig. 6).

287

288 **5. DISCUSSION**

289 *5.1 Comparison of SIMS and IRMS data*

290 The $\delta^{34}\text{S}$ and $\Delta^{33}\text{S}$ determined via SIMS and IRMS are consistent with $\delta^{34}\text{S}$ within 1\textperthousand
291 and $\Delta^{33}\text{S}$ within $0.5\text{\textperthousand}$ of each other (Fig. 7). Exceptions to this are for sulfides from the higher
292 grade (garnet and K-feldspar—sillimanite) samples where the IRMS data are offset to heavier
293 $\delta^{34}\text{S}$ values (by $1\text{--}2\text{\textperthousand}$, *c.f.*, SP-18-22 and SP-18-11, Fig. 7). This discrepancy is likely due to the
294 difficulties of analyzing pyrrhotite via SIMS (see section 4.3.1). Due the uncertainties with the

295 SIMS pyrrhotite data in the high-grade samples, we consider the bulk IRMS data to be most
296 reliable.

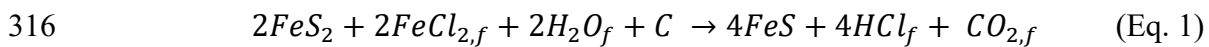
297

298 *5.2 Sulfur isotope fractionation during metamorphic devolatilization*

299 Metamorphic reactions involving the liberation of a fluid phase, particularly those
300 occurring at low temperatures, can drive large fractionations (≥ 1 to $10s \text{ ‰}$) of light stable
301 isotopes (*c.f.*, Rumble, 1982). Compared to other major fluid-mobile species, fractionation of
302 sulfur isotopes during metamorphism has been comparatively less studied (*e.g.*, Hall et al., 1988;
303 Oliver et al., 1992; Alirezaei and Cameron, 2001; Wagner and Boyce, 2006) and dominantly
304 through bulk (whole-rock or separated sulfide) analyses of natural samples [though see Alirezaei
305 and Cameron (2001) and Wagner and Boyce (2006) as examples of in-situ studies]. In addition,
306 these studies focused on either the effects of diagenesis (*i.e.*, pyrite formation and re-
307 precipitation; Wagner and Boyce, 2006), high-grade metamorphic rocks (Alirezaei and Cameron,
308 2001), retrograde metamorphism (Hall et al., 1988), or sulfidic black shales (Oliver et al., 1992).

309 The main sulfide reaction during prograde metamorphism is decomposition of pyrite to
310 pyrrhotite beginning at $\sim 200^\circ\text{C}$ (lower greenschist facies) and completing at $\sim 400^\circ\text{C}$ (upper
311 amphibolite facies) (Toulmin and Barton, 1964; Ferry, 1981; Tomkins, 2010). Two classes of
312 reactions may be involved in the reduction of sulfur and oxidation of another phase during pyrite
313 decomposition to pyrrhotite (see discussion of Ferry, 1981). First, there are those that require
314 iron addition to the sulfide mineral from either a free fluid phase:

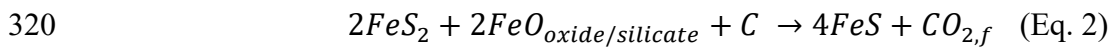
315



317

318 or a coexisting oxide or silicate phase:

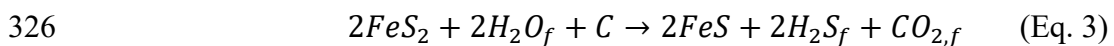
319



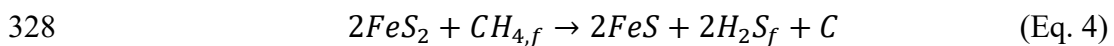
321

322 where the subscript *f* indicates a component in a free fluid. Both Equations 1 and 2 involve
323 oxidation of reduced carbon (*i.e.*, graphite) to CO₂. Second, there are reactions involving loss of
324 sulfur to a fluid phase:

325



327



329

330 Although Ferry (1981) determined that sulfur loss to fluid (Eqs. 3 and 4) predominated during
331 pyrite decomposition using bulk-rock Fe/S ratios and Fe/Mg ratios in co-existing biotite, that
332 study focused on graphitic sulfide-rich schists where the majority of iron and sulfur in the rocks
333 was contained within sulfides. In the relatively sulfide-poor schists studied here, sulfides are a
334 minor phase (<5 modal %) and pyrite breakdown reactions are neither the dominant control on
335 bulk-rock nor mineral compositional trends. Therefore, we are unable to constrain the specific
336 pyrite decomposition reaction. However, field studies (Ferry, 1981) and modeling (Tomkins,
337 2010) have demonstrated the importance of sulfur loss to a fluid phase during dehydration
338 reactions resulting from low pressure—high temperature metamorphism. For example, chlorite
339 breakdown and H₂O release during greenschist to amphibolite facies metamorphic conditions

340 drives pyrite breakdown because sulfur addition to the free fluid phase is required to maintain
341 equilibrium fluid compositions of H₂S, SO₂, and H₂O (Tomkins, 2010).

342 Although we cannot pinpoint the reaction resulting in pyrrhotite formation in our rocks,
343 we model the effects of sulfur-loss on the isotopic composition of metamorphic sulfides to
344 quantify maximum possible effects. At the low oxygen fugacity (f_{O_2}) and pH characteristic of
345 graphite-bearing metapelites, fluids will be H₂S-rich under metamorphic conditions (Poulson and
346 Ohmoto, 1989). For example, a COHS-bearing fluid in equilibrium with graphite, pyrite, and
347 pyrrhotite at 300 to 500°C and 0.3 GPa will be dominated by H₂O, H₂S, and CH₄. For this
348 reason, we do not calculate fluid speciation along a prograde path. We model sulfur isotope
349 fractionation during prograde desulfidation (Eq. 3 or 4) assuming an open system involving three
350 sulfur-bearing phases (H₂S, FeS₂, and FeS; Kajiwara et al., 1981):

351

352
$$\ln(R_{FeS_2}) - \ln(R_{FeS_2}^0) = \left[\frac{\alpha_1 - \alpha_2}{2} - 1 \right] * \ln(X) \quad (\text{Eq. 5})$$

353

354 where X is the extent of reaction expressed in terms of the molecular fraction of residual pyrite,
355 R^0 and R are ³⁴S/³²S isotope ratios of pyrite initially and at reaction extent X (0 to 1), and α_1 and
356 α_2 are the fractionation factors between H₂S-FeS₂ and FeS-FeS₂, respectively, defined as:

357

358
$$\alpha_1 = \frac{R_{H_2S}}{R_{FeS_2}} \quad (\text{Eq. 6a})$$

359

360
$$\alpha_2 = \frac{R_{FeS}}{R_{FeS_2}} \quad (\text{Eq. 6b})$$

361

362 Temperature-dependent values of α_1 and α_2 used in the model are given in Table S6 (Ohmoto
363 and Goldhaber, 1997). Desulfidation is assumed to follow mass dependent fractionation laws and
364 therefore ^{33}S is not considered in the model. An initial pyrite $\delta^{34}\text{S}$ value of -1.4‰ was used based
365 on the lowest sample-average $\delta^{34}\text{S}$ value from the biotite-chlorite grade. The full model is
366 available in Table S6.

367 Figure 8 shows the results of desulfidation modeling for temperatures of 200, 300, and
368 400°C. As H_2S and FeS in equilibrium with pyrite are depleted in ^{34}S , pyrite becomes
369 progressively heavier as the reaction proceeds, whereas FeS and H_2S produced from the reaction
370 are initially lighter than the initial pyrite ($X = 0-0.6$). For example, at 200°C, the first pyrrhotite
371 produced through desulfidation is depleted by 1.5‰ compared to the initial pyrite. At reaction
372 completion at 300-400°C, both H_2S and pyrrhotite are isotopically heavier than initial pyrite
373 reaching values of 0-2‰ (+2.6-4.6‰ above that of the initial pyrite). (Note: α_1 values used in
374 this modeling are < 1 , however Syverson et al. (2015) re-measured α_1 at 350°C and found it to
375 be > 1 , which would result in lower $\delta^{34}\text{S}$ values in pyrite than H_2S and reversing the sign of our
376 model results, *i.e.*, producing more negative residual pyrrhotite values. Thus, the Syverson et al.
377 α_1 may not apply here.)

378 As discussed above, our SIMS and IRMS datasets, while mostly in agreement,
379 demonstrate more significant differences for the high-grade (garnet to sillimanite-grade)
380 samples, with the IRMS $\delta^{34}\text{S}$ values being higher than respective SIMS values (Fig. 7). The
381 SIMS data suggests that prograde metamorphism did not significantly disturb the $\delta^{34}\text{S}$ of sulfides
382 in the metasedimentary rocks with most samples being within 1-2‰ of 0 (Fig. 5). In contrast, our
383 limited, but more precise IRMS dataset demonstrates a shift to heavier isotopic values in the
384 garnet and K-feldspar—sillimanite grade samples ($\delta^{34}\text{S} = +1-2\text{‰}$) by 2-3‰ from the biotite-

385 chlorite and andalusite grade samples ($\delta^{34}\text{S} = -1$ to $-2\text{\textperthousand}$). This observation can be explained
386 through removal of isotopically light H_2S during prograde metamorphism which would increase
387 residual pyrrhotite $\delta^{34}\text{S}$ values by 3 - 4\textperthousand at high grades (Fig. 8). It is also possible that there was
388 pre-metamorphic $\delta^{34}\text{S}$ heterogeneity among samples. Although we are unable to rule out this
389 possibility, among the 7 biotite-chlorite grade samples analyzed, most analyses ($\sim 93\%$) have
390 $\delta^{34}\text{S} < 0.5\text{\textperthousand}$. Last, $\Delta^{33}\text{S}$ shows no systematic trends with metamorphic grade, varying within
391 $0.5\text{\textperthousand}$ of 0 (Fig. 7), suggesting that S-MIF signatures were heterogeneous, but broadly conserved
392 during prograde metamorphism.

393

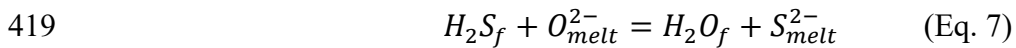
394 *5.3 Transfer of sulfur from metasedimentary rocks to granitic melts during anatexis*

395 Three of the four analyzed granite samples have $\delta^{34}\text{S}$ values heavier (by 1 - 2\textperthousand) than that
396 of the biotite-chlorite grade metasedimentary sulfides, but similar values to that of the $\delta^{34}\text{S}$ IRMS
397 values of pyrrhotite from high-grade (garnet and K-feldspar sillimanite) sedimentary rocks,
398 suggesting that the $\delta^{34}\text{S}$ of the granites reflect that of high-grade metasedimentary rocks affected
399 by metamorphic desulfidation reactions (see section 5.2). In reduced systems, where
400 desulfidation is driven primarily by the decomposition of pyrite to pyrrhotite, this will drive
401 positive, but small (on the order to $+2$ - 3\textperthousand) fractionations upon reaction completion. Importantly,
402 however, the granites preserve positive $\Delta^{33}\text{S}$ within the range of values observed in their
403 sedimentary source rocks (IRMS $\Delta^{33}\text{S}$ of 0.08 and $0.16\text{\textperthousand}$, Fig. 6 and 7b). To our knowledge,
404 this is the first study demonstrating non-zero $\Delta^{33}\text{S}$ in Archean granitic rocks (*sensu stricto*). Only
405 a handful of Archean igneous rocks have been shown to have non-zero $\Delta^{33}\text{S}$, including sulfides
406 from komatiite-hosted Ni deposits ($\Delta^{33}\text{S} = -1.0$ to $+2.6$; Bekker et al., 2009) and ultramafic sills,

407 gabbros, and tonalites from Nuvvuagittuq Greenstone Belt ($\Delta^{33}S = -0.03$ to $+0.18$; Thomassot et
408 al., 2015; Fig. 1c).

409 Granite sample SP-16-22 is an outlier, displaying negative and heterogeneous *in-situ* $\delta^{34}S$
410 (0 to $-16\text{\textperthousand}$). This sample is from part of the GLB characterized by abundant metasedimentary
411 inclusions (Fig. 2a,f). On a macroscopic level this indicates significant heterogeneity in the
412 granite and also, potentially, incomplete homogenization of the sulfur between the
413 metasedimentary rocks and granitic melt. During assimilation of metasedimentary host rock, the
414 metasedimentary sulfides break down upon heating and release H_2S (Eq. 3 & 4). (H_2S – as
415 opposed to SO_2 – would be the dominant gas phase under the low f_{O_2} of formation of the GLB;
416 Bucholz et al., 2018; Ohmoto, 1972; Poulson and Ohmoto, 1989). H_2S is transferred from the
417 fluid to the melt through the following reaction:

418



420

421 At oxygen fugacities near the graphite-CO buffer characteristic for the GLB (Bucholz et
422 al., 2018) sulfide (S^{2-}) in a hydrous melt may be complexed as either SH^- , H_2S , or FeS (e.g.,
423 Klimm et al., 2012). The low, heterogeneous $\delta^{34}S$ values in SP-16-22 as compared to the other
424 granites is likely due to fractionation between $\text{H}_2\text{S}_{\text{fluid}}$ and reduced sulfur species in the melt.
425 Although not constrained for rhyolitic melts at low ($<900^\circ\text{C}$) temperatures, existing experimental
426 data suggests that $\alpha(\text{H}_2\text{S}_{\text{fluid}} - \text{S}^{2-}_{\text{melt}})$ is >1 for basalt and andesite at 1030 - 1050°C
427 (summarized in Fiege et al., 2015). Therefore, the $\delta^{34}S$ of the fluid phase will be higher than the
428 sulfur dissolved in the melt. Figure 6b shows the $\delta^{34}S$ fractionation between $\text{H}_2\text{S}_{\text{fluid}}$ and $\text{S}^{2-}_{\text{melt}}$
429 using empirical fractionation factors of Fiege et al. (2015) (their Eq. 8) for basaltic and andesitic

430 melts extrapolated to 650-900°C. The $\delta^{34}\text{S}$ fractionation between $\text{H}_2\text{S}_{\text{fluid}}$ and $\text{S}^{2-}_{\text{melt}}$ at 1030°C is
431 4.6-5.0‰ and will increase at lower temperatures (Fiege et al., 2015). These calculations
432 demonstrate that H_2S in the fluid may be 5-10‰ heavier than S^{2-} in the melt over the temperature
433 range expected for the crystallization of a hydrous granitic melt. Therefore, the isotopically light
434 and heterogeneous nature of the sulfides may be the result of incomplete homogenization
435 between isotopically light H_2S derived from pyrite decomposition in the metasedimentary
436 inclusions and the granitic melt prior to solidification. S^{2-} diffusion in hydrous (7 wt.% H_2O)
437 rhyolitic melts is several orders of magnitude slower than other volatile species (Baker and
438 Rutherford, 1996), which would serve to preserve sulfur isotopic heterogeneity in a melt during
439 assimilation. For example, at 800°C sulfur requires $\sim 10^3$ years to equilibrate over 10 cm in a
440 hydrous rhyolitic melt (using diffusivities of Baker and Rutherford, 1996). Notably, diffusion
441 induced fractionation of ^{34}S and ^{32}S is minimal in basaltic melts (*i.e.*, the diffusivities of ^{34}S and
442 ^{32}S are similar; Fortin et al., 2019) and, if we assume that this finding can be applied for high-
443 silica melts, the intrasample $\delta^{34}\text{S}$ variability in sulfides is likely not due to diffusive fractionation.
444

445 *5.4 SPGs as a record of the bulk siliciclastic Archean sedimentary sulfur reservoir*

446 This work demonstrates that the sulfur isotopic composition of SPGs mirrors the $\delta^{34}\text{S}$ of
447 their high-grade metasedimentary source rocks (within $\sim 1\text{‰}$) and is similar to that of low grade
448 source rocks, shifted at most $+2\text{-}3\text{‰}$ (Fig. 5). Prograde pyrite breakdown results in residual
449 sulfide in metasedimentary rocks that have higher $\delta^{34}\text{S}$ than the original pyrite. This elevated
450 $\delta^{34}\text{S}$ is then transferred to the granitic melts during partial melting. Although heterogeneous and
451 low $\delta^{34}\text{S}$ in one granitic sample suggests inefficient homogenization of sulfur may occur, most
452 pyrite from the granites display homogeneous values in agreement with bulk sulfide $\delta^{34}\text{S}$ via

453 IRMS. Thus, $\delta^{34}\text{S}$ of SPGs should broadly reflect that of their source sediments and
454 inhomogeneity can be screened for through in-situ analyses of sulfides.

455 Second, small (tenths of ‰) positive $\Delta^{33}\text{S}$ observed in the metasedimentary rocks are
456 also observed in the GLB granites, suggesting the transfer and preservation of S-MIF through
457 metamorphism and partial melting. As a cautionary note, however, the absence of S-MIF in
458 igneous rocks does not preclude assimilation of Archean sedimentary material (although this has
459 been previously implied, *c.f.* LaFlamme et al. 2018; Smit et al. 2019). This can arise in several
460 instances: (1) The majority of Archean sedimentary sulfides do not preserve significant S-MIF
461 (Fig. 1a,b) and therefore partial melting or assimilation of these sources would not result in S-
462 MIF in magmatic products; (2) The partial melting/assimilation of a sedimentary rock package
463 with both positive and negative $\Delta^{33}\text{S}$ could result in a bulk $\Delta^{33}\text{S}$ of 0 in the melt; and (3)
464 Dilution by external non-MIF-bearing sulfur could obscure S-MIF imparted to the magmas by
465 sedimentary assimilation.

466 Our observations demonstrate that Archean SPGs provide a useful archive for
467 understanding the Archean sulfur cycle. As Archean SPGs are generated under reducing
468 conditions similar to that of the GLB (Bucholz et al., 2018), we suggest that the $\delta^{34}\text{S}$ and $\Delta^{33}\text{S}$ of
469 Archean SPGs could provide an estimate of the bulk siliciclastic source rock from which they
470 were derived. A survey of sulfur isotopes of global Archean SPGs (*c.f.* localities in Bucholz and
471 Spencer, 2019) could provide an alternative archive to sedimentary rocks in that they average out
472 small spatial heterogeneities often sampled in sedimentary studies. The SPG sulfur isotope
473 record would be particularly useful in light of studies suggesting that Archean crust is not mass
474 balanced in terms of sulfur with its bulk $\Delta^{33}\text{S}$ being skewed to positive values (Farquhar and
475 Wing, 2003; Reinhard et al., 2013) instead of being similar to that of bulk Earth ($\Delta^{33}\text{S} = 0$;

476 Labidi et al., 2013). The idea that the Archean crust has a bulk composition $\Delta^{33}S > 0$ is based on
477 compilations of $\Delta^{33}S$ in Archean sedimentary rocks that are skewed towards positive values
478 (e.g., Johnston et al., 2011). The complementary negative $\Delta^{33}S$ reservoir has been suggested to
479 be deeply subducted hydrothermally-altered oceanic crust that acquired its sulfur from the
480 oceanic sulfate reservoir (Cabral et al., 2013; Farquhar et al., 2002). In contrast, Torres et al.
481 (2018) analyzed multiple sulfur isotopes of surface and ground waters draining bedrock of the
482 Superior craton and found that these waters had an average sulfur isotopic composition
483 equivalent to that of the bulk Earth ($\Delta^{33}S \approx 0$) suggesting that on average the bulk Archean crust
484 was mass balanced. Similarly, SPGs would provide a more direct, integrated record of Archean
485 crustal sulfur over large volumes of supracrustal rocks, and could serve as an archive that isolates
486 the bulk Archean sedimentary reservoir, rather than a mixture of igneous (*i.e.*, mafic volcanic
487 rocks and granitoids) and sedimentary rocks that define Archean terranes.

488

489 *5.5 Implications for using sulfur isotopes as a tracer of Archean sedimentary material in the*
490 *mantle*

491 One of the most exciting recent applications of sulfur isotopes in the igneous record is the
492 identification of S-MIF in mantle-derived igneous rocks: sulfides from some ocean island basalts
493 (Cabral et al., 2013; Delavault et al., 2016; green dots in Fig. 1c) and diamonds (Farquhar et al.,
494 2002; Cartigny et al., 2009; Thomassot et al., 2009; Smit et al. 2019; red dots in Fig. 1c), as well
495 as in bulk-rock analyses of Proterozoic plutonic rocks (Selvaraja et al., 2017; LaFlamme et al.,
496 2018; blue dots in Fig. 1c). These observations have been interpreted to suggest that sulfur
497 processed through the Archean atmosphere was transferred into the deep Earth through
498 subduction. Our specific case study interrogates the transfer of sedimentary sulfur to the igneous

499 rock record (*i.e.*, through direct partial melting of Archean sedimentary rocks to produce SPGs)
500 to understand this process in its most fundamental form. We demonstrate that during
501 metamorphism and partial melting within the upper crust, reduced Archean metasedimentary
502 rocks and their derivative granites should preserve (within a few ‰) the original $\delta^{34}\text{S}$ and $\Delta^{33}\text{S}$
503 of their protoliths if not modified by an external sulfur source.

504 Assuming subduction (or a variant of it) operated in the Archean, subducted altered
505 oceanic crust and sediments would have been relatively reduced as compared to present day
506 (*e.g.*, Evans, 2012; Stolper and Bucholz, 2019) and the main reservoir of sulfur in subducting
507 slabs would be pyrite in sediments or volcanogenic deposits and magmatic pyrrhotite in mid-
508 ocean ridge basalts (or gabbros). Thus, sulfur transfer to the mantle wedge would occur through
509 pyrite/pyrrhotite decomposition and H_2S release (Jégo and Dasgupta, 2013). As this process
510 results in relatively little fractionation (at most a few per mil) at elevated temperatures ($>200^\circ\text{C}$,
511 see section 5.2), subduction of Archean sedimentary (and igneous) sulfides which have $\delta^{34}\text{S}$ at or
512 near 0‰ (Fig. 1b) should result in release of H_2S in the mantle wedge with a similar value.
513 Residual sulfides that were then deeply subducted would have a similar to slightly heavier $\delta^{34}\text{S}$.
514 Our study also suggests that S-MIF (if initially present) should be preserved during
515 devolatilization and partial melting as long as it is not diluted by an external source of sulfur.
516 Although some studies have suggested that subducted Archean slabs would carry a negative
517 $\Delta^{33}\text{S}$ signature due to sulfate incorporation (*e.g.*, Cabral et al., 2013; Delavault et al., 2016),
518 sulfate concentrations in the Archean ocean were low ($<200 \mu\text{mol}$) (Canfield and Farquhar,
519 2009) and consequently sulfur concentrations in hydrothermally altered oceanic crust derived
520 from oceanic sulfate were also low. Alternatively, in situations where pyrite-bearing sediment

521 fluxes to subduction zones were low, Archean arc magmas or slab melts may have had sulfur
522 isotopic compositions similar to that of the mantle ($\delta^{34}\text{S} \approx -1$; $\Delta^{33}\text{S} = 0$; Labidi et al., 2013).

523 Therefore, Archean subduction likely transferred distinct sulfur isotopic and redox
524 signatures to arc-related magmas as compared to modern day. In the Archean, primitive arc
525 basalts or slab melts were likely relatively reduced (*i.e.*, similar to mid-ocean ridge basalts
526 (MORB) or potentially more reduced; Stolper and Bucholz, 2019) and characterized by $\delta^{34}\text{S}$ near
527 0 and possibly non-zero $\Delta^{33}\text{S}$. In contrast, present day arc basalts are generally oxidized
528 compared to MORB due to subduction of Fe^{3+} - and sulfate-bearing sediments and
529 hydrothermally altered oceanic crust (*c.f.*, Evans, 2012) and have variable, though generally
530 positive $\delta^{34}\text{S}$ (and $\Delta^{33}\text{S} = 0$). Although it is beyond the scope of this paper to fully discuss
531 modern day sulfur cycling in subduction zones, the positive $\delta^{34}\text{S}$ have been interpreted as
532 evidence of sulfur transfer to the mantle wedge through subduction of sulfur derived from the
533 oceanic sulfate pool (*c.f.*, Wallace and Edmonds, 2011). In addition, sulfur isotope fractionation
534 during sulfide/sulfate metamorphism and fluid release in modern subducting slabs is potentially
535 more significant (as compared to reduced slabs in the Archean) due to the present of multiple
536 sulfur redox species in minerals and fluids (Walters et al., 2019; Li et al., 2020).

537

538 **6. Conclusions**

539 We demonstrate that during metamorphism and partial melting, reduced Archean
540 metasedimentary rocks and their derivative granites should closely retain the original sulfur
541 isotope composition of their protoliths if not modified by an external sulfur source. $\delta^{34}\text{S}$ values
542 from the GLB and surrounding metasedimentary rock, as well as modeling results indicate that
543 prograde metamorphic pyrite desulfidation reactions can drive residual pyrrhotite to isotopically

544 heavier values by at most 2-3‰ over a temperature range of 200-400°C. Furthermore, the $\delta^{34}\text{S}$
545 values of pyrite from SPGs of the GLB closely resemble that of pyrrhotite in their high-grade
546 metasedimentary source rocks. One exception to this is a granite sample demonstrating intra-
547 sample pyrite sulfur isotope disequilibrium likely resulting from incomplete homogenization
548 between sulfur derived from a metasedimentary-derived fluid and granitic melt.

549 Sulfides from both the granites and the metasedimentary rocks preserve similar, non-zero
550 $\Delta^{33}\text{S}$ values. Notably, however, $\Delta^{33}\text{S}$ values are within several tenths of a permil of 0 and only
551 identifiable with high-precision IRMS analyses. Importantly, however, the absence of S-MIF in
552 igneous rocks does not exclude the assimilation of Archean sedimentary material. Igneous rocks
553 without S-MIF, but with Archean surface-derived sulfur could form through a variety of non-
554 exclusive processes: (1) assimilation or partial melting of Archean sulfur with $\Delta^{33}\text{S}=0$; (2) partial
555 melting/assimilation of sulfur with a bulk $\Delta^{33}\text{S}$ of 0; and (3) dilution by external sulfur with zero
556 $\Delta^{33}\text{S}$.

557 SPGs are a potential archive of the bulk sulfur isotopic composition of Archean
558 siliciclastic sedimentary rocks averaged over large volumes. Further, mass transfer of sulfur from
559 the sedimentary to igneous rock record explored here is likely applicable to subduction scenarios.
560 In the Archean sulfur transfer from the slab to the mantle wedge would occur through
561 pyrite/pyrrhotite decomposition and H_2S release. As this process results in relatively small
562 fractionation (at most a few per mil) at elevated temperatures, subduction of Archean
563 sedimentary (and igneous) sulfides which have $\delta^{34}\text{S}$ at or near 0‰ should result in release of
564 sulfur in the mantle wedge with a similar value. S-MIF (if initially present in the subducted
565 Archean surface material) should be preserved during this process as long as it is not diluted by
566 external sulfur (e.g., from the mantle).

567

568 **Acknowledgements**

569 We thank Madeline Lewis and Allyson Trussell for help collecting samples, Yunbin
570 Guan for assistance with SIMS analyses, and Gareth Izon for assistance with the IRMS analyses.
571 C. Bucholz thanks Fred Breaks for spending time in the field introducing her to the Ghost Lake
572 batholith, John Eiler for discussion of sulfur isotope analyses via SIMS, and Doug Crowe and
573 Woody Fischer for generously providing sulfide standard materials. This work was supported by
574 NSF grant EAR-1943629 awarded to C. Bucholz. We are grateful for the comments of two
575 anonymous reviewers which help to clarify and improve the presentation of this work.

576

577

578

579

580 REFERENCES

581 Alirezaei, S., Cameron, E.M., 2001. Variations of sulfur isotopes in metamorphic rocks from Bamble
582 Sector, southern Norway: a laser probe study. *Chemical Geology* 181, 23–45. doi:10.1016/S0009-
583 2541(01)00266-2

584 Beaudry, P., Longpré, M.A., Economos, R., Wing, B.A., Bui, T.H. and Stix, J., 2018. Degassing-induced
585 fractionation of multiple sulphur isotopes unveils post-Archaean recycled oceanic crust signal in
586 hotspot lava. *Nature Communications* 9(1), 1-12.

587 Bekker, A., Barley, M.E., Fiorentini, M.L., Rouxel, O.J., Rumble, D., Beresford, S.W., 2009.
588 Atmospheric Sulfur in Archean Komatiite-Hosted Nickel Deposits. *Science* 326, 1086–1089.
589 doi:10.1126/science.1177742

590 Blackburn, C.E., Johns, G.W., Ayer, J.A., Davis, D.W., 1991. The Wabigoon Subprovince, in: *Geology*
591 of Ontario, The Wabigoon Subprovince. *Geology of Ontario*. Ontario Geological Survey, pp. 303–382.

592 Breaks, F.W., Moore, J.M., 1992. The Ghost Lake Batholith, Superior Province of Northwestern Ontario:
593 A Fertile, S-Type, Peraluminous Granite - Rare-Element Pegmatite System. *Canadian Mineralogist* 30,
594 835–875.

595 Bucholz, C.E., Spencer, C.J., 2019. Strongly Peraluminous Granites across the Archean–Proterozoic
596 Transition. *Journal of Petrology* 60, 1299–1348. doi:10.1093/petrology/egz033

597 Bucholz, C.E., Stolper, E.M., Eiler, J.M., Breaks, F.W., 2018. A Comparison of Oxygen Fugacities of
598 Strongly Peraluminous Granites across the Archean–Proterozoic Boundary. *Journal of Petrology* 59,
599 2123–2156. doi:10.1093/petrology/egy091

600 Cabral, R.A., Jackson, M.G., Rose-Koga, E.F., Koga, K.T., Whitehouse, M.J., Antonelli, M.A., Farquhar,
601 J., Day, J.M.D., Hauri, E.H., 2013. Anomalous sulphur isotopes in plume lavas reveal deep mantle
602 storage of Archean crust. *Nature* 496, 490–493. doi:10.1038/nature12020

603 Canfield, D.E., 2004. The Early History of Atmospheric Oxygen. *Annual Reviews in Earth and Planetary
604 Sciences*, 33, 1–36. doi:10.1146/annurev.earth.33.092203.122711

605 Canfield, D.E., Farquhar, J., 2009. Animal evolution, bioturbation, and the sulfate concentration of the

606 oceans. PNAS 106, 8123–8127. doi:10.1073/pnas.0902037106

607 Canfield, D.E., Raiswell, R., Westrich, J.T., Reaves, C.M., Berner, R.A., 1986. The use of chromium
608 reduction in the analysis of reduced inorganic sulfur in sediments and shales. Chem. Geol. 54, 149–
609 155. [https://doi.org/10.1016/0009-2541\(86\)90078-1](https://doi.org/10.1016/0009-2541(86)90078-1).

610 Cartigny, P., Farquhar, J., Thomassot, E., Harris, J.W., Wing, B., Masterson, A., McKeegan, K. and
611 Stachel, T., 2009. A mantle origin for Paleoarchean peridotitic diamonds from the Panda kimberlite,
612 Slave Craton: evidence from ^{13}C -, ^{15}N -and $^{33},^{34}\text{S}$ -stable isotope systematics. *Lithos*, 112, pp.852-864.

613 Craig, J.R. and Vokes, F.M., 1993. The metamorphism of pyrite and pyritic ores: an
614 overview. *Mineralogical Magazine*, 57(386), 3-18.

615 Crowe, D.E., Vaughan, R.G., 1996. Characterization and use of isotopically homogeneous standards for
616 in situ laser microprobe analysis of $^{34}\text{S}/^{32}\text{S}$ ratios. *American Mineralogist* 81, 187–193.
617 doi:10.2138/am-1996-1-223

618 Cui, H., Kitajimai, K., Spicuzza, M.J., Fournelle, J.H., Ishida, A., Brown, P.E., Valley, J.W., 2018.
619 Searching for the Great Oxidation Event in North America: A Reappraisal of the Huronian Supergroup
620 by SIMS Sulfur Four-Isotope Analysis. *Astrobiology* 18, 519–538. doi:10.1089/ast.2017.1722

621 Delavault, H., Chauvel, C., Thomassot, E., Devey, C.W., Dazas, B., 2016. Sulfur and lead isotopic
622 evidence of relic Archean sediments in the Pitcairn mantle plume. PNAS 113, 12952–12956.
623 doi:10.1073/pnas.1523805113

624 Dottin III, J.W., Labidi, J., Lekic, V., Jackson, M.G. and Farquhar, J., 2020. Sulfur isotope
625 characterization of primordial and recycled sources feeding the Samoan mantle plume. *Earth and*
626 *Planetary Science Letters* 534, 116073.

627 Evans, K.A., 2012. The redox budget of subduction zones. *Earth-Science Reviews* 113, 11–32.
628 doi:10.1016/j.earscirev.2012.03.003

629 Farquhar, J., Wing, B., 2003. Multiple sulfur isotopes and the evolution of the atmosphere. *Earth and*
630 *Planetary Science Letters* 213, 1–13.

631 Farquhar, J., Wing, B.A., McKeegan, K.D., Harris, J.W., Cartigny, P., Thiemens, M.H., 2002. Mass-

632 Independent Sulfur of Inclusions in Diamond and Sulfur Recycling on Early Earth. *Science* 298,
633 2369–2372. doi:10.1126/science.1078617

634 Ferry, J.M., 1981. Petrology of graphitic sulfide-rich schists from south-central Maine: an example of
635 desulfidation during prograde regional metamorphism. *American Mineralogist* 66, 908–930.

636 Fiege, A., Holtz, F., Behrens, H., Mandeville, C.W., Shimizu, N., Crede, L.S., Göttlicher, J., 2015.
637 Experimental investigation of the S and S-isotope distribution between $\text{H}_2\text{O}-\text{S} \pm \text{Cl}$ fluids and basaltic
638 melts during decompression. *Chemical Geology* 393-394, 36–54. doi:10.1016/j.chemgeo.2014.11.012

639 Fischer, W.W., Fike, D.A., Johnson, J.E., Raub, T.D., Guan, Y., Kirschvink, J.L. and Eiler, J.M., 2014.
640 SQUID–SIMS is a useful approach to uncover primary signals in the Archean sulfur
641 cycle. *Proceedings of the National Academy of Sciences* 111(15), 5468-5473.

642 Fortin, M.A., Watson, E.B., Stern, R.A. and Ono, S., 2019. Experimental characterization of diffusive and
643 Soret isotopic fractionation of sulfur in a reduced, anhydrous basaltic melt. *Chemical Geology* 510, 10-
644 17.

645 Halevy, I., Johnston, D.T. and Schrag, D.P., 2010. Explaining the structure of the Archean mass-
646 independent sulfur isotope record. *Science* 329(5988), 204-207.

647 Hall, A.J., Boyce, A.J., Fallick, A.E., 1988. A Sulphur Isotope Study of Iron Sulphides in the Late
648 Precambrian Dalradian Easdale Slate Formation, Argyll, Scotland. *Mineral. Mag.* 52, 483–490.
649 doi:10.1180/minmag.1988.052.367.06

650 Holdaway, M.J., 2000. Application of new experimental and garnet Margules data to the garnet-biotite
651 geothermometer. *American Mineralogist* 85, 881–892. doi:10.2138/am-2000-0701

652 Holtz, F., Johannes, W., Pichavant, M., 1992. Effect of excess aluminium on phase relations in the system
653 Qz-Ab-Or: experimental investigation at 2 kbar and reduced H_2O -activity. *Eur.J.Mineral.* 4, 137–152.

654 Ishihara, S., Sasaki, A., 1989. Sulfur isotopic ratios of the magnetite-series and ilmenite-series granitoids
655 of the Sierra Nevada batholith—A reconnaissance study. *Geology* 17, 788–791. doi:10.1130/0091-
656 7613(1989)017<0788:SIROTM>2.3.CO;2

657 Jégo, S., Dasgupta, R., 2013. Fluid-present melting of sulfide-bearing ocean-crust: Experimental
658 constraints on the transport of sulfur from subducting slab to mantle wedge. *Geochimica et
659 Cosmochimica Acta* 110, 106–134. doi:10.1016/j.gca.2013.02.011

660 Johnston, D.T., 2011. Multiple sulfur isotopes and the evolution of Earth's surface sulfur cycle. *Earth
661 Science Reviews* 106(1-2), 161-183.

662 Kajiwara, Y., Sasaki, A., Matsubara, O., 1981. Kinetic sulfur isotope effects in the thermal decomposition
663 of pyrite. *Geochem. J.* 15, 193–197. doi:10.2343/geochemj.15.193

664 Klimm, K., Kohn, S.C., Botcharnikov, R.E., 2012. The dissolution mechanism of sulphur in hydrous
665 silicate melts. II: Solubility and speciation of sulphur in hydrous silicate melts as a function of fO₂.
666 *Chemical Geology* 322-323, 250–267. doi:10.1016/j.chemgeo.2012.04.028

667 Kozdon, R., Kita, N.T., Huberty, J.M., Fournelle, J.H., Johnson, C.A., Valley, J.W., 2010. In situ sulfur
668 isotope analysis of sulfide minerals by SIMS: Precision and accuracy, with application to thermometry
669 of ~ 3.5 Ga Pilbara cherts. *Chemical Geology* 275, 243–253. doi:10.1016/j.chemgeo.2010.05.015

670 Labidi, J., Cartigny, P., Moreira, M., 2013. Non-chondritic sulphur isotope composition of the terrestrial
671 mantle. *Nature* 501, 208–211. doi:10.1038/nature12490

672 Labidi, J., Cartigny, P. and Jackson, M.G., 2015. Multiple sulfur isotope composition of oxidized Samoan
673 melts and the implications of a sulfur isotope ‘mantle array’ in chemical geodynamics. *Earth and
674 Planetary Science Letters* 417, 28-39.

675 LaFlamme, C., Fiorentini, M.L., Lindsay, M., Bui, T.H., 2018. Atmospheric sulfur is recycled to the
676 crystalline continental crust during supercontinent formation. *Nature Communications* 9, 4380.

677 Li, J.L., Schwarzenbach, E.M., John, T., Ague, J.J., Huang, F., Gao, J., Klemd, R., Whitehouse, M.J. and
678 Wang, X.S., 2020. Uncovering and quantifying the subduction zone sulfur cycle from the slab
679 perspective. *Nature Communications* 11(1), 1-12.

680 Magalhães, N., Penniston-Dorland, S., Farquhar, J. and Mathez, E.A., 2018. Variable sulfur isotope
681 composition of sulfides provide evidence for multiple sources of contamination in the Rustenburg
682 Layered Suite, Bushveld Complex. *Earth and Planetary Science Letters* 492, 163-173.

683 Magalhães, N., Farquhar, J., Bybee, G., Penniston-Dorland, S., Rumble III, D., Kinnaird, J. and
684 McCreesh, M., 2019. Multiple sulfur isotopes reveal a possible non-crustal source of sulfur for the
685 Bushveld Province, southern Africa. *Geology* 47(10), 982-986.

686 Ohmoto, H., Goldhaber, M.B., 1997. Isotopes of sulfur and carbon, in: Barnes, H.L. (Ed.), *Geochemistry*
687 of Hydrothermal Ore Deposits. John Wiley & Sons, pp. 491–559.

688 Oliver, N.H.S., Hoering, T.C., Johnson, T.W., Rumble, D., III, Shanks, W.C., III, 1992. Sulfur isotopic
689 disequilibrium and fluid-rock interaction during metamorphism of sulfidic black shales from the
690 Waterville-Augusta area, Maine, USA. *Geochimica et Cosmochimica Acta* 56, 4257–4265.
691 doi:10.1016/0016-7037(92)90266-L

692 Ono, S., 2017. Photochemistry of sulfur dioxide and the origin of mass-independent isotope fractionation
693 in Earth's atmosphere. *Annual Reviews of Earth and Planetary Sciences* 45, 301–329.
694 doi:10.1146/annurev-earth-060115-012324

695 Ono, S., Wing, B., Johnston, D., Farquhar, J. and Rumble, D., 2006. Mass-dependent fractionation of
696 quadruple stable sulfur isotope system as a new tracer of sulfur biogeochemical cycles. *Geochimica et*
697 *Cosmochimica Acta*, 70(9), pp.2238-2252.

698 Ono, S., Keller, N.S., Rouxel, O., Alt, J.C., 2012. Sulfur-33 constraints on the origin of secondary pyrite
699 in altered oceanic basement. *Geochim. Cosmochim. Acta* 87, 323–340.
700 <https://doi.org/10.1016/j.gca.2012.04.016>

701 Penniston-Dorland, S.C., Wing, B.A., Nex, P.A., Kinnaird, J.A., Farquhar, J., Brown, M. and Sharman,
702 E.R., 2008. Multiple sulfur isotopes reveal a magmatic origin for the Platreef platinum group element
703 deposit, Bushveld Complex, South Africa. *Geology* 36(12), 979-982.

704 Penniston-Dorland, S.C., Mathez, E.A., Wing, B.A., Farquhar, J. and Kinnaird, J.A., 2012. Multiple
705 sulfur isotope evidence for surface-derived sulfur in the Bushveld Complex. *Earth and Planetary*
706 *Science Letters* 337, 236-242.

707 Poulson, S.R., Ohmoto, H., 1989. Devolatilization equilibria in graphite-pyrite-pyrrhotite bearing pelites
708 with application to magma-pelite interaction. *Contrib Mineral Petrol* 101, 418–425.

709 doi:10.1007/BF00372215

710 Reinhard, C.T., Planavsky, N.J., Lyons, T.W., 2013. Long-term sedimentary recycling of rare sulphur
711 isotope anomalies. *Nature* 497, 100–103. doi:10.1038/nature12021

712 Rumble, D., 1982. Stable isotope fractionation during metamorphic devolatilization reactions. *Reviews in*
713 *Mineralogy and Geochemistry* 10(1), 327-353.

714 Selvaraja, V., Fiorentini, M.L., LaFlamme, C.K., Wing, B.A. and Bui, T.H., 2017. Anomalous sulfur
715 isotopes trace volatile pathways in magmatic arcs. *Geology* 45(5), 419-422.

716 Smit, K.V., Shirey, S.B., Hauri, E.H., Stern, R.A., 2019. Sulfur isotopes in diamonds reveal differences in
717 continent construction. *Science* 364, 383–385. doi:10.1126/science.aaw9548

718 Stolper, D.A., Bucholz, C.E., 2019. Neoproterozoic to early Phanerozoic rise in island arc redox state due
719 to deep ocean oxygenation and increased marine sulfate levels. *PNAS* 116, 8746–8755.
720 doi:10.1073/pnas.1821847116

721 Syverson, D.D., Ono, S., Shanks, W.C. and Seyfried Jr, W.E., 2015. Multiple sulfur isotope fractionation
722 and mass transfer processes during pyrite precipitation and recrystallization: an experimental study at
723 300 and 350°C. *Geochimica et Cosmochimica Acta* 165, 418-434.

724 Thomassot, E., Cartigny, P., Harris, J.W., Lorand, J.P., Rollion-Bard, C., Chaussidon, M., 2009.
725 Metasomatic diamond growth: A multi-isotope study (^{13}C , ^{15}N , ^{33}S , ^{34}S) of sulphide inclusions and
726 their host diamonds from Jwaneng (Botswana). *Earth and Planetary Science Letters* 282, 79–90.
727 doi:10.1016/j.epsl.2009.03.001

728 Thomassot, E., O’Neil, J., Francis, D., Cartigny, P. and Wing, B.A., 2015. Atmospheric record in the
729 Hadean Eon from multiple sulfur isotope measurements in Nuvvuagittuq Greenstone Belt (Nunavik,
730 Quebec). *Proceedings of the National Academy of Sciences* 112(3), 707-712.

731 Thompson, A.B., Tracy, R.J., 1979. Model systems for anatexis of pelitic rocks: II. Facies Series Melting
732 and Reaction in the System $\text{CaO}-\text{KAlO}_2-\text{NaAlO}_2-\text{Al}_2\text{O}_3-\text{SiO}_2-\text{H}_2\text{O}$ *Contrib Mineral Petrol* 70: 429-
733 438.

734 Tomkins, A.G., 2010. Windows of metamorphic sulfur liberation in the crust: Implications for gold

735 deposit genesis. *Geochimica et Cosmochimica Acta* 74, 3246–3259. doi:10.1016/j.gca.2010.03.003

736 Torres, M.A., Paris, G., Adkins, J.F., Fischer, W.W., 2018. Riverine evidence for isotopic mass balance in
737 the Earth's early sulfur cycle. *Nature Geosciences* 11, 661–664. doi:10.1038/s41561-018-0184-7

738 Toulmin, P., III, Barton, P.B., Jr., 1964. A thermodynamic study of pyrite and pyrrhotite. *Geochimica et*
739 *Cosmochimica Acta* 28, 641–671. doi:10.1016/0016-7037(64)90083-3

740 Wagner, T., Boyce, A.J., 2006. Pyrite metamorphism in the Devonian Hunsrück slate of Germany:
741 Insights from laser microprobe sulfur isotope analysis and thermodynamic modeling. *American*
742 *Journal of Science* 306, 525–552.

743 Wallace, P.J. and Edmonds, M., 2011. The sulfur budget in magmas: evidence from melt inclusions,
744 submarine glasses, and volcanic gas emissions. *Reviews in Mineralogy and Geochemistry*, 73(1), 215–
745 246.

746 Walters, J.B., Cruz-Uribe, A.M. and Marschall, H.R., 2019. Isotopic compositions of sulfides in exhumed
747 high-pressure terranes: implications for sulfur cycling in subduction zones. *Geochemistry, Geophysics,*
748 *Geosystems* 20(7), 3347-3374.

749

750

751

752 **FIGURE CAPTIONS**

753

754 **Figure 1:** Comparison of triple S isotope data of this study with sedimentary and selected igneous studies.755 A) $\Delta^{33}\text{S}$ versus $\delta^{34}\text{S}$ for Archean sedimentary sulfides (compilation of Johnston (2011). B)756 Histograms of $\delta^{34}\text{S}$ (left panel) and $\Delta^{33}\text{S}$ (right panel) for same compilation shown in A. C) $\Delta^{33}\text{S}$ 757 versus $\delta^{34}\text{S}$ for sulfides from various studies including: Archean komatiite-hosted Fe-Ni sulfide

758 deposits (Bekker et al., 2009); meta-igneous ultramafic, gabbroic, and tonalitic rocks (Thomassot et

759 al., 2015); bulk-rock data for Proterozoic (~1620-1820 Ma) Moorarie and Durlacher Supersuites

760 (plutonic rocks) from the Capricorn orogen in Australia (LaFlamme et al., 2018); pegmatites and

761 tonalites from the Glenburgh arc (2.0 Ga), Australia (Selvaraja et al., 2017); range of bulk-rock and

762 sulfide data from the 2.06 Ga Bushveld Complex (blue field; Penniston-Dorland et al., 2008; 2012;

763 Magaelhães et al., 2018; 2019); sulfide inclusions in diamonds (Farquhar et al., 2002; Cartigny et al.,

764 2009; Thomassot et al., 2009; Smit et al., 2019); sulfide inclusions in olivines, clinopyroxene, or

765 spinel from ocean island basalts (Cabral et al., 2013; Delevault et al., 2016; Beaudry et al., 2018);

766 bulk-rock data for OIBs and hot spots (Labidi et al., 2013; 2015; Dottin et al., 2020). Depleted MORB

767 end-member is from Labidi et al. (2013). The method of analysis is given in legend – SIMS or IRMS.

768 Error bars were omitted for clarity, but vary widely by study and analysis type and the reader is

769 referred to the original references for more detail. Broadly, however, reported SIMS measurements

770 have $2\sigma \delta^{34}\text{S}$ uncertainties from tenths to $>1\text{\textperthousand}$ and $2\sigma \Delta^{33}\text{S}$ uncertainties of 0.1-0.4‰. Corresponding771 values for IRMS measurements are several 0.1-0.6‰ and <0.01 to 0.09‰, respectively.

772

773 **Figure 2:** (A) Geologic map of the Ghost Lake batholith (GLB) modified from Breaks and Moore, 1992.

774 Sample prefixes of “SP-” are omitted for clarity. Hatched area indicates inclusion rich zone of

775 batholith. Unit GLB-8 described in text is not shown as it comprises 3-8 cm pegmatitic dikes. (B-F)

776 field photos from the GLB. Hammer head is 13.5 cm long. Locations where photos were taken are

777 shown as yellow stars in (A). (B) cm-scale cordierite porphyroblasts aligned along foliation from

778 metapelite above the andalusite isograd (photo location: N49°45'55.6" W093°06'46.9") (C) metapelite
779 and metagraywacke beds above the andalusite isograd. Andalusite porphyroblasts occur in the
780 metapelites, but not in the metagreywackes (photo location: N49°46'49.8" W092°49'46.1"). Sharpie is
781 14 cm long. (D) Biotite+plagioclase+quartz gneiss with fine-grained leucosomes above sillimanite-K-
782 feldspar isograd (photo location: N49°48'54.9", W093°09'34.6") (E) biotite-rich metapelite with
783 nebulous boundary with pegmatitic granite (photo location: N49°50'50.9", W092°41'31.0") (F) coarse-
784 grained biotite-muscovite granite with biotite-rich metapelitic inclusion and late-stage tourmaline-
785 bearing dikes (photo location: N49°48'53.7", W092°57'04.7")
786

787 **Figure 3:** Photomicrographs of A) pyrrhotite (po) and chalcopyrite (ccp) in sample SP-18-11 a
788 metagraywacke from the sillimanite-K-feldspar isograd and B) pyrite in sample E19-8 a
789 biotite+muscovite granite. Images are reflected light and red circle highlight sulfides.
790

791 **Figure 4:** Pressure-temperature conditions of metamorphism for the Zealand metasedimentary unit.
792 Isograds shown in different colors. The granite solidi are from Holtz et al. (1992). The pyrophyllite
793 dehydration reaction is from Kerrick (1968) and the muscovite dehydration reaction is from
794 Thompson and Tracy (1979). Mineral abbreviations: AS = aluminosilicate, Kfs = K-feldspar, Ky =
795 kyanite, Mu = muscovite, Pl = plagioclase, Prl = pyrophyllite, Q = quartz, Sil = sillimanite, f = fluid.
796

797 **Figure 5:** Histograms of $\delta^{34}\text{S}$ (‰) of sulfides from biotite-chlorite (A), andalusite (B), garnet (C), and K-
798 feldspar—sillimanite (D) grade metamorphic rocks and peraluminous granite samples (E). Histograms
799 show $\delta^{34}\text{S}$ values obtained via SIMS. (Note: only samples for which SIMS data could be confidently
800 corrected to a matrix matched standards are shown.) Colored horizontal bars show average plus one
801 standard deviation in $\delta^{34}\text{S}$ values for specific samples. Circles show $\delta^{34}\text{S}$ values obtained via IRMS for
802 seven samples.
803

804 **Figure 6:** A) $\Delta^{33}\text{S}$ versus $\delta^{34}\text{S}$ of pyrite from peraluminous granites. Grey symbols indicate SIMS values
805 (with 1σ) and black symbols indicate IRMS values. B) Calculated fractionation between H_2S in a fluid
806 and S^{2-} in a melt based on rhyolite fractionation factors given in Fiege et al. (2015) over the range of
807 650-900°C. For example, an H_2S -bearing fluid with a $\delta^{34}\text{S}$ value of 0‰ will be in equilibrium with S^{2-}
808 in a rhyolitic melt with a $\delta^{34}\text{S}$ value of approximately -10‰ at 650°C.

809

810 **Figure 7:** Comparison of $\delta^{34}\text{S}$ (A) and $\Delta^{33}\text{S}$ (B) obtained via SIMS and IRMS. For SIMS values, sample
811 average value is shown with 1σ standard deviation on average.

812

813 **Figure 8:** Results of Rayleigh fractionation modeling for $\delta^{34}\text{S}$ during pyrite desulfidation (Eq. 8).
814 Calculated for 200, 300, and 400 °C (left to right panels). Fractionation factors from Ohmoto and
815 Goldhaber (1997). Initial pyrite value (red line) at -1.4‰ is based on lower limit observed in chlorite-
816 grade samples. Shifting the initial pyrite value to a higher value would shift modeled curves upwards
817 by an equal amount. Gray bar indicates the range of $\delta^{34}\text{S}$ of sulfides (as obtained via IRMS) observed
818 in garnet- and K-feldspar-sillimanite grade metasedimentary rocks.

819